J Adv Ceram

Research Article

Mechanism of improved breakdown strength and energy storage performance in Cd-doped $Sr_{0.775}Bi_{0.15}TiO_3$ relaxor ferroelectrics based on a multi-scale synergistic optimization strategy

Peng Zhao[1,2,3], Yubin Liu[4], Jingjing Chen[5,6], Yongjia Zhang[4], Bo Chen[4], Yinhui Li[7], Chenguang Niu[1], Xiaoyan Xiong[1], Yongzhen Wang[2], Bin Tang[8,9]

Cite this article: Zhao P, Liu Y, Chen J, et al. *J Adv Ceram* 2026, **15**(6): 9221314. https://doi.org/10.26599/JAC.2026.9221314

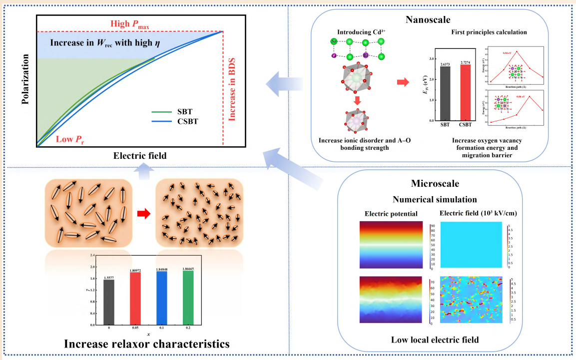

ABSTRACT: $Sr_{0.775}Bi_{0.15}TiO_3$ ceramics with linear-like relaxor ferroelectric behavior are promising dielectric energy storage materials. Improving breakdown strength (BDS) is key to optimizing its energy storage performance and expanding its application. Herein, a multi-scale synergistic optimization strategy is employed by introducing Cd^{2+} in $Sr_{0.775}Bi_{0.15}TiO_3$ ceramics to improve the BDS and energy storage performance, and the underlying mechanism of performance optimization is systematically investigated. At the nanoscale, first-principles calculations combined with electrical testing and structural characterization reveal that Cd^{2+} doping increases the ionic disorder, A–O bond strength, and the formation energy and migration barrier of oxygen vacancies. This inhibits oxygen vacancy transport and enhances electrical insulation. At the microscale, numerical simulations verify that the composition with appropriate doping exhibits a small and uniform local electric field. This decreases the breakdown probability. Meanwhile, Cd^{2+} doping enhances relaxor ferroelectricity. Consequently, the BDS is improved while maintaining low remnant polarization, and the optimized $Cd_{0.05}Sr_{0.725}Bi_{0.15}TiO_3$ ceramic exhibits excellent comprehensive energy storage performance with a high recoverable energy density of 5.16 J/cm³ and an efficiency of 92.65 % under 490 kV/cm. The performance possesses outstanding stability over a broad temperature range (21–150 °C), a wide frequency range (10–1000 Hz), and up to 10^5 charge–discharge cycles. This sample also shows a high-power density of 115.02 MW/cm³ and an ultrafast discharge time of 0.046 μs. Therefore, $Cd_{0.05}Sr_{0.775}Bi_{0.15}TiO_3$ ceramic is promising for advanced pulsed-power capacitor applications, and this work provides additional mechanisms and strategic guidance for improving BDS and energy storage performance of linear-like relaxor ferroelectrics.

KEYWORDS: energy storage performance; lead-free ceramics; oxygen vacancy; electrical properties; $Sr_{0.775}Bi_{0.15}TiO_3$ (SBT)

1 Introduction

With the rapid development of modern society, environmental pollution and energy scarcity have become increasingly severe, making the development of renewable energy and energy storage particularly important [1]. Among various energy storage devices, dielectric capacitors offer distinct advantages, including ultrafast charge–discharge kinetics, extended cycle life, and high power density [2]. These characteristics render them indispensable in applications ranging from medical devices and exhaust

---

[1] College of Robotics Science and Engineering, Taiyuan University of Technology, Taiyuan 030024, China. [2] College of Materials Science and Engineering, Taiyuan University of Technology, Taiyuan 030024, China. [3] School of Integrated Circuit Science and Engineering, University of Electronic Science and Technology of China, Chengdu 611731, China. [4] College of Physics and Optoelectronics, Taiyuan University of Technology, Taiyuan 030024, China. [5] College of Computer Science and Engineering, Guilin University of Technology, Guilin 541006, China. [6] College of Materials Science and Engineering, Guilin University of Technology, Guilin 541004, China. [7] College of Integrated Circuits, Taiyuan University of Technology, Taiyuan 030024, China. [8] National Engineering Research Center of Electromagnetic Radiation Control Materials, University of Electronic Science and Technology of China, Chengdu 611731, China. [9] National Key Laboratory of Electronic Thin Films and Integrated Devices, University of Electronic Science and Technology of China, Chengdu 611731, China.

Corresponding authors. E-mail: P. Zhao, itceozp@126.com; J. Chen, chenjingjing@glut.edu.cn; Y. Wang, wangyongzhen@tyut.edu.cn; B. Tang, tangbin@uestc.edu.cn

Received: March 10, 2026; Revised: April 21, 2026; Accepted: May 2, 2026

purification systems to defense technologies [2–4]. The dielectric energy storage performance, including the energy storage density (W), recoverable energy storage density (W_{rec}), and energy storage efficiency (η), can be quantitatively evaluated using established theoretical equations (Eqs. (1)–(3)):

$$W=\int_0^{P_{\max}} E\mathrm{d}P \tag{1}$$

$$W_{\mathrm{rec}}=\int_{P_{\mathrm{r}}}^{P_{\max}} E\mathrm{d}P \tag{2}$$

$$\eta=\frac{W_{\mathrm{rec}}}{W}\times 100\% \tag{3}$$

where $P_{\max}$ is the maximum polarization; P_{r} is the remanent polarization; E is the electric field. Therefore, the combination of a large polarization difference ($P_{\max}$–P_{r}) and a high breakdown strength (BDS) is beneficial for obtaining high W_{rec} and η in dielectric materials. Among them, the BDS is the core parameter that determines the W_{rec}, power output capability, and high-voltage service boundary of dielectric energy storage materials. A higher BDS value is more conducive to achieving higher energy storage performance and to meeting more demanding high-voltage application scenarios.

Dielectric materials can be categorized into four main types: linear dielectrics, ferroelectrics, anti-ferroelectrics, and relaxor ferroelectrics [5–9]. Among them, relaxor ferroelectrics possess a higher BDS than conventional ferroelectrics and anti-ferroelectrics, a higher $P_{\max}$ than linear dielectrics, a lower P_{r} than ferroelectrics, and excellent fatigue resistance compared with anti-ferroelectrics, making them highly promising for advanced energy storage applications [10]. Relaxor ferroelectrics typically originate from conventional ferroelectrics (such as $\mathrm{Bi_{0.5}Na_{0.5}TiO_3}$, $\mathrm{BiFeO_3}$, and $\mathrm{BaTiO_3}$) doped with aliovalent ions. This induces polar nanoregions (PNRs), thereby achieving relaxor ferroelectric properties. However, excessively high P_{r} in ferroelectrics often makes it difficult to achieve high η, which is detrimental to obtaining excellent comprehensive energy storage performance and the operational stability and reliability of energy storage devices.

$\mathrm{(Sr,Bi)TiO_3}$ is a kind of lead-free relaxor ferroelectric system derived from Bi-doped linear dielectric $\mathrm{SrTiO_3}$ and exhibits distinctive quasilinear polarization behavior characterized by low dielectric loss, low P_{r}, high η, suitable relative dielectric constant, and polarity [11]. These factors give $\mathrm{(Sr,Bi)TiO_3}$ ceramics significant application potential in high-frequency and high-voltage environments of advanced pulse power systems. However, compared with other relaxor ferroelectrics, $\mathrm{(Sr,Bi)TiO_3}$ ceramics have a relatively low BDS, which directly limits W_{rec} and the upper limit of its tolerance to the operating electric field. Therefore, improving the BDS of $\mathrm{(Sr,Bi)TiO_3}$ ceramics by controlling the microstructure through ion doping is a key approach to overcoming the performance limit and expanding the application of high-voltage pulse power.

In recent years, researchers have employed a variety of strategies (grain refinement, resistance increase, volatilization inhibition, etc.) to improve the BDS of $\mathrm{(Sr,Bi)TiO_3}$ ceramics [12–18]. Li *et al.* [14] prepared $\mathrm{Sr_{0.7}Bi_{0.2}Ti_{1-1.25\mathit{x}}Nb_{\mathit{x}}O_3}$ ceramics. The insulation of the sample was improved by reducing the grain size, resulting in an enhanced BDS and achieving a W_{rec} of 3.43 J/cm^3 with an η of 85.84% at 385 kV/cm. However, since heterovalent doping at the B site creates structural vacancies, which promote the formation of oxygen vacancies and a second phase, it reduces electrical conductivity and limits further improvement of BDS. Meanwhile, the vibrations between B-site atoms and O atoms are related to the polarity and dynamics of PNRs [19]. B-site doping with non-ferroelectric active ions in $\mathrm{(Sr,Bi)TiO_3}$ can easily lead to a significant decrease in $P_{\max}$. Chen *et al.* [12,13] replaced $\mathrm{Bi^{3+}}$ with rare earth ions to compensate for ion vacancies caused by elemental volatilization, which improved the resistivity and BDS. The prepared $\mathrm{Sr_{0.7}Bi_{0.15}Re_{0.05}TiO_3}$ (Re: Yb and Ho) ceramics exhibit a W_{rec} of 2.16–2.32 J/cm^3 with an η of 92.2%–95.8% at 300 kV/cm. However, the excessive heterovalent ions and structural vacancies at the A-site promote the formation of the second phase, limiting further improvements in resistivity and BDS. The existing literatures largely focus on improving insulation to enhance BDS, but research on the conductivity mechanism is generally insufficient. While a few studies have focused on oxygen vacancy-dominated conductivity behavior, only the regulation of oxygen vacancy concentration has been emphasized, neglecting the migration characteristics. This results in an incomplete BDS optimization mechanism based on oxygen vacancy transport dynamics, and there are few studies on $\mathrm{(Sr,Bi)TiO_3}$ ceramics that combine BDS > 450 kV/cm, W_{rec} > 5 J/cm^3, and η > 90%. Therefore, precise strategy design based on this mechanism is crucial and necessary for optimizing the energy storage performance of $\mathrm{(Sr,Bi)TiO_3}$ ceramics.

In this work, to maintain high polarity and mitigate element volatilization and the formation of oxygen vacancies and secondary phases caused by high $\mathrm{Bi^{3+}}$ content (the solid solution limit of Bi in $\mathrm{(Sr,Bi)TiO_3}$ ceramics is 20 mol% [20]), $\mathrm{Sr_{0.775}Bi_{0.15}TiO_3}$ (SBT) is selected as the base material. $\mathrm{Cd^{2+}}$ is a non-volatile ion with a small radius and large polar displacement, which can effectively increase local ionic disorder to hinder oxygen vacancy migration and reduce cell volume to enhance A–O bonds and reduce oxygen vacancy formation in the A-site of perovskite ceramics [21–26]. Therefore, the isovalent substitution of $\mathrm{Sr^{2+}}$ by $\mathrm{Cd^{2+}}$ in SBT is expected to significantly improve BDS while maintaining high $P_{\max}$ and low P_{r} by optimizing oxygen vacancy transport and microstructure, thereby achieving comprehensive energy storage performance. Based on these results, a multi-scale synergistic optimization strategy based on $\mathrm{Cd_{\mathit{x}}Sr_{0.775-\mathit{x}}Bi_{0.15}TiO_3}$ ceramics is proposed to improve the BDS and energy storage performance and elucidate the optimization mechanisms. At the nanoscale, $\mathrm{Cd^{2+}}$ doping decreases the lattice volume and enhances ionic disorder and A–O bond strength. These suppress the formation and migration of oxygen vacancies, as evidenced by characterization tests and by first-principles calculations of the changes in oxygen vacancy formation and migration energy, thereby enhancing electrical insulation properties. At the microscale, appropriate doping forms pure-phase ceramics with high electrical homogeneity, which exhibit a low, uniform local electric field (LEF) according to numerical simulations. The relaxor ferroelectricity of SBT ceramics is enhanced after doping. Consequently, W_{rec} is significantly improved by enhancing BDS while maintaining high $\mathrm{P_{max}}$, low P_{r} and high η. As a result, the $\mathrm{Cd_{0.05}Sr_{0.775}Bi_{0.15}TiO_3}$ ceramic achieves a high W_{rec} of 5.16 J/cm^3 and a high η of 92.65% at a high electric field of 490 kV/cm. Meanwhile, this sample exhibits a high power density of 115.02 MW/cm^3 and excellent temperature, frequency, and cycle stability in energy storage performance. $\mathrm{Cd_{0.05}Sr_{0.775}Bi_{0.15}TiO_3}$ ceramics demonstrate great potential for pulsed power energy storage applications owing to their excellent comprehensive energy storage performance.

2 Experimental

High-purity $\mathrm{SrCO_3}$, $\mathrm{Bi_2O_3}$, $\mathrm{TiO_2}$, and CdO powders were used as raw materials, and $\mathrm{Cd_{\mathit{x}}Sr_{0.775-\mathit{x}}Bi_{0.15}TiO_3}$ (defined as CSBT100x, x = 0, 0.05, 0.1, and 0.2) ceramics were synthesized via the conventional solid-state reaction method [24,27]. Raw materials were weighed in a stoichiometric ratio. The prepared mixed powder was ball-milled in ethyl alcohol using zirconia balls for 8 h. Then, the slurry was dried and presented at 950 °C for 3 h in air. After that, the powder was ball-milled in ethyl alcohol using zirconia balls for 4 h. The slurry was dried and mixed with a 10 wt% solution of polyvinyl alcohol (PVA), and the powder was pressed into disks of 10 mm diameter, 1 mm thick at 10 MPa. Finally, the disks buried in the stabilized ZrO_2 powders were heat-treated at 600 °C for 2 h to remove PVA and sintered at 1220–1260 °C for 3 h in air. The samples used for the dielectric property test and the complex impedance test were fully covered with Ag electrodes. The silver pastes were coated on both sides of the sample, and the silver electrodes were fired at 620 °C for 30 min. The samples used for the ferroelectric test and charge–discharge test were polished to a thickness of 0.05–0.08 mm and covered with an Au electrode with a 2 mm diameter. Gold electrodes were deposited on both sides of the sample using a benchtop ion sputtering system.

An X-ray diffractometer (XRD) with Cu Kα radiation (X'Pert Pro MPD, PANalytical, Netherlands) and a Raman spectrometer (RENISHAW, In Via reflex, UK) under 514.5 nm laser excitation were used to test the crystalline structure of the samples. A field-emission scanning electron microscope (SEM; ZEISS GeminiSEM 300, Germany) was used to observe the micromorphology of the samples. An LCR meter (Agilent E4980A, USA) was used to measure the temperature- and frequency-dependent dielectric properties and the complex impedance of the samples. X-ray photoelectron spectroscopy (XPS) was conducted by a Thermo Scientific K-Alpha spectrometer. The polarization–electric field (*P*–*E*) hysteresis loops, the current density–electric field (*J*–*E*) loops, and the leakage current density were tested using a ferroelectric test system (FETS-2000, Wuhan Yanhe Technology Co., Ltd., China). A commercial charge–discharge platform (CFD-003, Tongguo (TG) technology, China) was used to test the charging and discharging properties of the samples.

3 Results and discussion

3.1 Crystal structure and micromorphology analyses of CSBT

Figure 1 presents XRD patterns of the CSBT ceramics. The main phase of all samples is perovskite structure ($SrTiO_3$, PDF#00-35-0734). The compositions with x = 0 and 0.05 exhibit pure phase structures. However, secondary phases are identified as $Bi_2Ti_2O_7$, Sr_2TiO_4, and $Cd_{0.8}Sr_{0.2}TiO_3$ for $x \geq 0.1$. The absence of splitting in the (111) and (200) diffraction peaks confirms pseudocubic symmetry. A systematic shift of the diffraction peaks toward higher 2θ angles is observed with increasing x, signifying a decrease in both lattice parameters and unit cell volume. This lattice contraction results from the substitution of the larger Sr^{2+} ions (1.44 Å, coordination number (CN) 12) by smaller Cd^{2+} ions (1.31 Å, CN 12) at the A-site of the perovskite lattice [28].

Raman spectroscopy further elucidates the structural evolution. The spectra, deconvoluted using Gaussian–Lorentzian mixed functions to resolve individual vibrational modes, are presented in Fig. 2(a). The wavenumbers in Fig. 2(b) are read from the deconvoluted results for each sample. Due to overlapping modes and ionic disorder, all compositions exhibit broad Raman bands [29]. Modes below 200 cm^{-1} correspond to A-site cation vibrations [29]. The Sr–O vibration peak near 146 cm^{-1} exhibits an overall blueshift trend with increasing doping content x, which can be attributed to the displacement of A-site ions induced by Cd^{2+} doping [30]. The mode at approximately 193 cm^{-1} gradually becomes sharper as x increases. This is mainly attributed to the increase in Cd–O bonds after the introduction of Cd^{2+}. Vibrations associated with B–O bonds and BO_6 octahedra are observed in the ranges of 200–400 and 400–700 cm^{-1}, respectively [31]. The Raman modes near 303 cm^{-1} undergo redshifts, indicating the formation of a weakly polar pseudo-cubic relaxation structure [32–34]. Meanwhile, the Raman peaks related to the oxygen octahedron gradually sharpened, indicating an oxygen octahedral distortion. This phenomenon can be attributed to the increase in the degree of structural and ionic disorder, which means a reduction in the size of PNRs and an enhancement in relaxation properties.

The microstructural characteristics of the samples were characterized by SEM. Cross-sectional SEM images (Figs. 3(a)–3(d) and Fig. S1 in the Electronic Supplementary Material (ESM)) indicate that all compositions exhibit dense microstructural features. The distribution of the secondary phases is further clearly revealed by backscattered electron (BSE) images (Figs. 3(e) and 3(f)). No obvious secondary phase was observed for the composition with x = 0.05 in Fig. 3(e), whereas a distinct secondary phase (white regions) was observed for the composition with x = 0.2 in Fig. 3(f), which is consistent with the XRD results.

3.2 Dielectric property analyses of CSBT

The temperature-dependent dielectric properties of CSBT

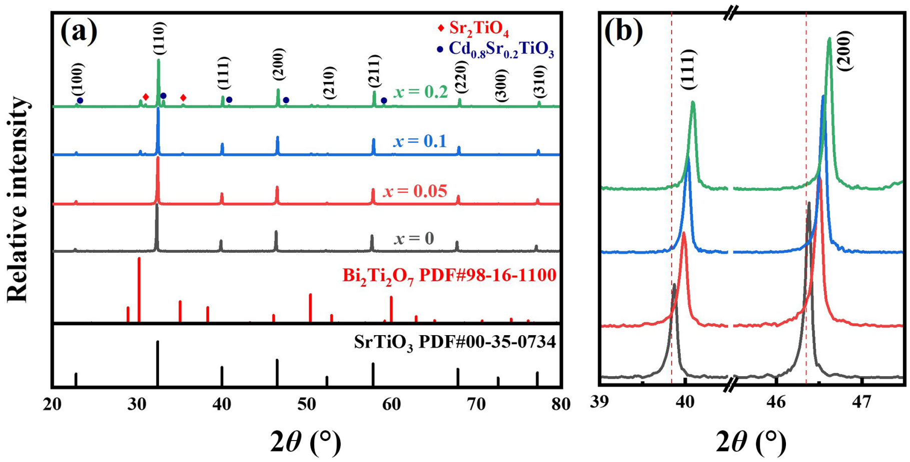

Fig. 1 (a) XRD patterns of $Cd_xSr_{0.775-x}Bi_{0.15}TiO_3$ (x = 0, 0.05, 0.1, and 0.2) ceramics. (b) Magnified (111) and (200) diffraction peaks of $Cd_xSr_{0.775-x}Bi_{0.15}TiO_3$ (x = 0, 0.05, 0.1, and 0.2).

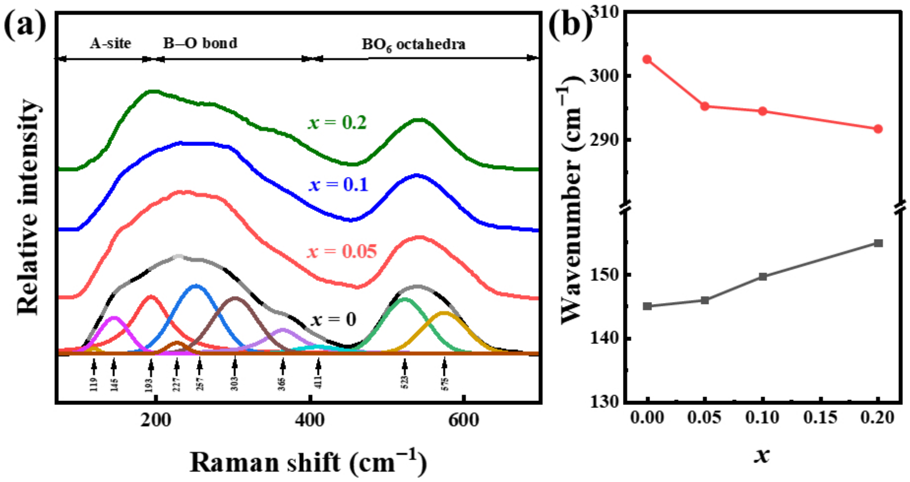

Fig. 2 (a) Raman spectra of $Cd_xSr_{0.775-x}Bi_{0.15}TiO_3$ (x = 0, 0.05, 0.1, and 0.2) as a function of the Cd content. (b) Variation of wavenumbers for some related Raman modes.

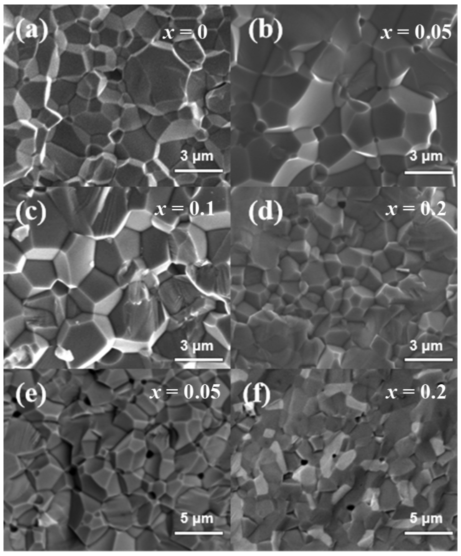

Fig. 3 (a–d) SEM images of cross section of $Cd_xSr_{0.775-x}Bi_{0.15}TiO_3$ (x = 0, 0.05, 0.1, and 0.2). (e–f) SEM images of cross section of $Cd_xSr_{0.775-x}Bi_{0.15}TiO_3$ (x = 0.05 and 0.2) in backscattered electron mode.

ceramics across various frequencies are displayed in Fig. 4 and Fig. S2 in the ESM. All samples show clear diffuseness and frequency dispersion, which are typical characteristics of relaxor ferroelectrics [35]. As x increases, the relative dielectric constant (ε_r) progressively decreases, primarily due to the greater disorder introduced by ion doping. This doping disrupts the long-range ordered structure and introduces a secondary phase with low ε_r forming, collectively lowering the overall ε_r. Furthermore, the dielectric peak broadens noticeably as x increases, indicating the increased chemical and structural disorder. This phenomenon results from the incorporation of Cd^{2+}, which enhances cation disorder at the A-site, leading to stronger compositional fluctuations and nanoscale structural inhomogeneity while also refining PNRs and creating variations in local polarization behavior.

The evolution of domain structures in relaxor ferroelectrics can be reflected via temperature-dependent ε_r. Characteristic temperatures, including the Freezing temperature (T_f), the temperature of maximum relative dielectric constant ε_m (T_m), and the Burns temperature (T_B), serve as key indicators of relaxor behavior, following the thermodynamic sequence $T_f < T_m < T_B$ [36]. Within the T_f–T_m range, submicron ferroelectric microdomains remain in the ceramics. When the temperature rises to the range of T_m–T_B, the polar structure transforms into nanodomains or PNRs. In the T_m–T_B range, the further the room temperature is from T_m, the smaller the size of the polar structures [37]. The decrease in T_m with increasing x further confirms the refinement of PNRs. This trend also reflects the enhanced ferroelectric instability and relaxor characteristics. The broadening of the dielectric peak further suggests improved dielectric temperature stability of the ceramics.

The degree of relaxation is a key parameter for quantifying the deviation of materials from normal ferroelectric behavior and characterizing their relaxor properties, as it reflects the dynamic disorder of PNRs. It can also be used to evaluate the broadening of the dielectric peak and is typically calculated using the modified Curie–Weiss law, as given by Eq. (4):

$$\frac{1}{\varepsilon} - \frac{1}{\varepsilon_m} = \frac{(T - T_m)^\gamma}{C} \tag{4}$$

where C corresponds to the Curie constant, and ε_m is the maximum ε_r. The parameter γ ranges from 1 for normal ferroelectrics to 2 for ideal relaxor ferroelectrics. The γ values for all samples, derived from the temperature-dependent ε_r at 100 kHz (Fig. S3 in the ESM), are presented in Fig. 4(a). As x increases, γ rises, indicating an enhanced relaxor behavior (Fig. 4(b)). This enhancement can be attributed to the increased ionic disorder resulting from the incorporation of Cd^{2+} into SBT lattice.

3.3 BDS and electrical conduction analyses of CSBT

The BDS is a critical parameter for affecting the energy storage performance of dielectric ceramics. As shown in Fig. 5(a), with increasing doping concentration x, the BDS rises from 310 kV/cm at x = 0 to 490 kV/cm at x = 0.05. The enhancement of BDS is influenced by multiple factors, including microstructural features (grain size, grain boundaries, and secondary phases) and electrical conductivity.

The complex alternating current (AC) impedance plots (Z'–Z'') of the CSBT ceramics are shown in Figs. 5(b)–5(e). As the temperature increases, the diameter of the semicircle gradually decreases, indicating a reduction in the resistance of the material. The direct current conductivity (σ_{DC}) of CSBT ceramics was obtained by fitting the impedance measurement results at different temperatures (Fig. 5(f)) and the conduction activation energy (E_{cond}) was calculated using the Arrhenius equation (Eq. (5)) to investigate the underlying conduction mechanism:

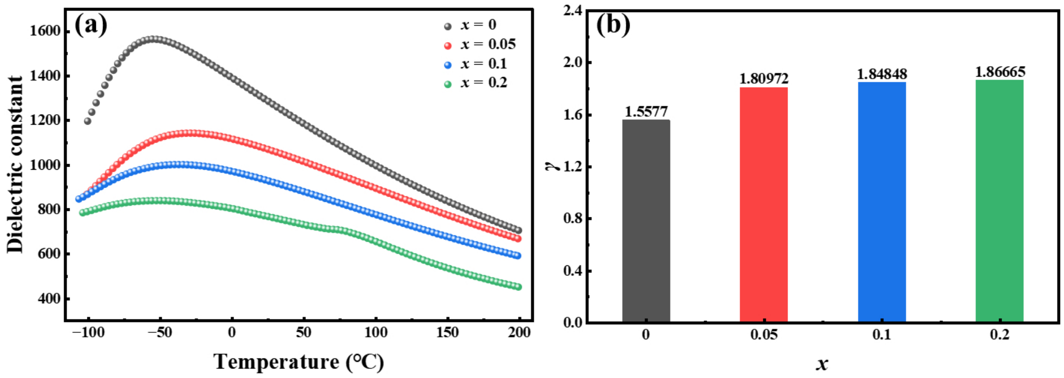

Fig. 4 (a) Temperature dependence of $(1-x)Sr_{0.775-x}Cd_xBi_{0.15}TiO_3$ (x = 0, 0.05, 0.1, and 0.2) ceramics with increasing x at −100–200 °C at 100 kHz. (b) Relaxor degree (γ) of $(1-x)Sr_{0.775-x}Cd_xBi_{0.15}TiO_3$ (x = 0, 0.05, 0.1, and 0.2) ceramics recorded at 100 kHz.

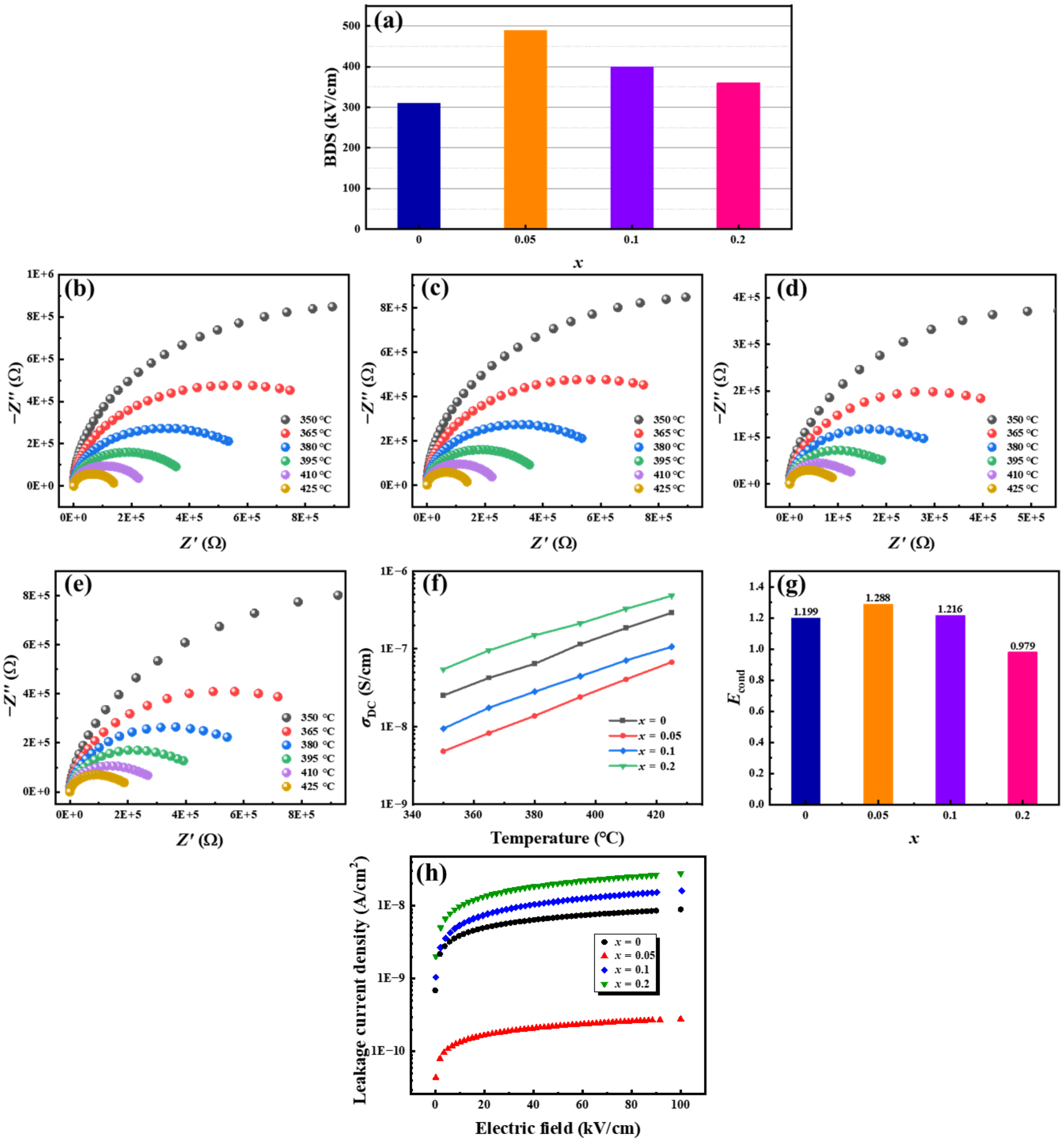

Fig. 5 (a) BDS values of $Cd_xSr_{0.775-x}Bi_{0.15}TiO_3$ (x = 0, 0.05, 0.1, and 0.2) ceramics. (b–e) Nyquist plots of impedance for $Cd_xSr_{0.775-x}Bi_{0.15}TiO_3$ (x = 0, 0.05, 0.1, and 0.2) ceramics at different temperatures and frequencies. (f) Temperature dependence of σ_{DC} for $Cd_xSr_{0.775-x}Bi_{0.15}TiO_3$ (x = 0, 0.05, 0.1, and 0.2) ceramics. (g) Temperature dependence of E_{cond} for $Cd_xSr_{0.775-x}Bi_{0.15}TiO_3$ (x = 0, 0.05, 0.1, and 0.2) ceramics. (h) Leakage current density versus electric field plots of $Cd_xSr_{0.775-x}Bi_{0.15}TiO_3$ (x = 0, 0.05, 0.1, and 0.2).

$$\sigma_{\mathrm{DC}} = \sigma_0 \exp\left(\frac{-E_{\mathrm{cond}}}{k_{\mathrm{b}}T}\right) \tag{5}$$

where k_b is the Boltzmann constant and σ_0 is the pre-exponential factor. All samples exhibit increasing σ_{DC} with increasing temperature, indicating the increased dynamics and concentration of the thermally activated charge carriers. The E_{cond} (Fig. 5(g) and Fig. S4 in the ESM) of all samples falls within the range of 0.5–2 eV, indicating the conduction mechanism dominated by oxygen vacancies [38]. As x increases from 0 to 0.05, E_{cond} gradually increases, σ_{DC} decreases, and the leakage current density decreases (Fig. 5(h)). This behavior can be attributed to the inhibition of oxygen vacancy transport, which is associated with changes in oxygen vacancy concentration and migration [39].

Oxygen vacancy concentration is a key factor affecting the electrical conductivity and BDS of CSBT ceramics. To explore the regulatory mechanism of Cd^{2+} doping on the formation of oxygen vacancies in CSBT ceramics, first-principles calculations calculation study based on density functional theory (DFT) was conducted. The Heyd–Scuseria–Ernzerhof hybrid functional (HSE06) was employed within a plane-wave computational framework for all simulations [40]. Figures 6(a) and 6(b) show the computational models used in this study (the model selection are provided in Figs. S5 and S6 in the ESM).

To ensure reliable energy convergence, the plane-wave cutoff energy was set to 400 eV, and the convergence criterion for electronic self-consistent field steps was fixed at 60 eV/cell. A 2 × 2 × 2 supercell was used for slab construction. For Brillouin zone sampling, the Monkhorst–Pack scheme was adopted with a 4 × 4 × 4 k-point mesh. All surface atoms were allowed to relax, and the structural relaxation process was terminated when the total energy variation was less than 1.0×10^{-6} eV/atom. The energy required to create an oxygen vacancy can be determined through Eq. (6) [41]:

$$E_{\mathrm{fV}} = E_{\mathrm{V}} - E_{\mathrm{tot}} + E_{\mathrm{O}} \tag{6}$$

where E_{fV} represents the oxygen vacancy formation energy, E_{V} denotes the total energy of the defect system containing a vacancy, E_{tot} corresponds to the total energy of the ideal pristine system, and E_{O} is the chemical potential of an isolated oxygen atom. The chemical potential is set with respect to the equilibrium gas state and takes half of the total energy of an O_2 molecule. In this case, this value is −4.388 eV [42]. According to the computational results, the E_{fV} of SBT is 2.6373 eV, whereas that of CSBT is 2.7274 eV (Fig. 6(c)). This indicates that the introduction of Cd^{2+} makes it more difficult to form oxygen vacancies, which is conducive to inhibiting the formation of oxygen vacancies.

The XPS spectra of the O 1s valence state for the samples with x = 0 and 0.05 are shown in Figs. 6(d) and 6(e). Three Gaussian–Lorentzian peaks are observed for all samples. Taking the x = 0 sample as an example, the lattice oxygen peak (peak I) locates at a lower binding energy of approximately 529.86 eV, the oxygen vacancy-related peak (peak II) locates at a higher binding energy of approximately 531.77 eV, and the peak at 532.88 eV corresponds to surface-adsorbed water (peak III) [43]. As x increases from 0 to 0.05, the area ratio of peak II to peak I decreases from 54.58% to 24.61%, confirming a reduction in the oxygen vacancy concentration. This consist with the calculation results and can be attributed to the lattice contraction induced by Cd^{2+} incorporation, which in turn increases E_{fV} and decreases the oxygen vacancy concentration.

The migration energy barrier of oxygen vacancies is another key factor affecting the electrical conductivity and BDS of CSBT ceramics. The migration pathways of oxygen vacancies and the associated energy barriers were determined by identifying the minimum energy paths (MEPs) between adjacent lattice sites using the nudged elastic band (NEB) method as implemented in Vienna *ab initio* simulation package (VASP) [44]. Initially, the two endpoint configurations (initial and final) corresponding to the vacancy states were obtained through separate ionic relaxation calculations with full optimization. A set of intermediate atomic

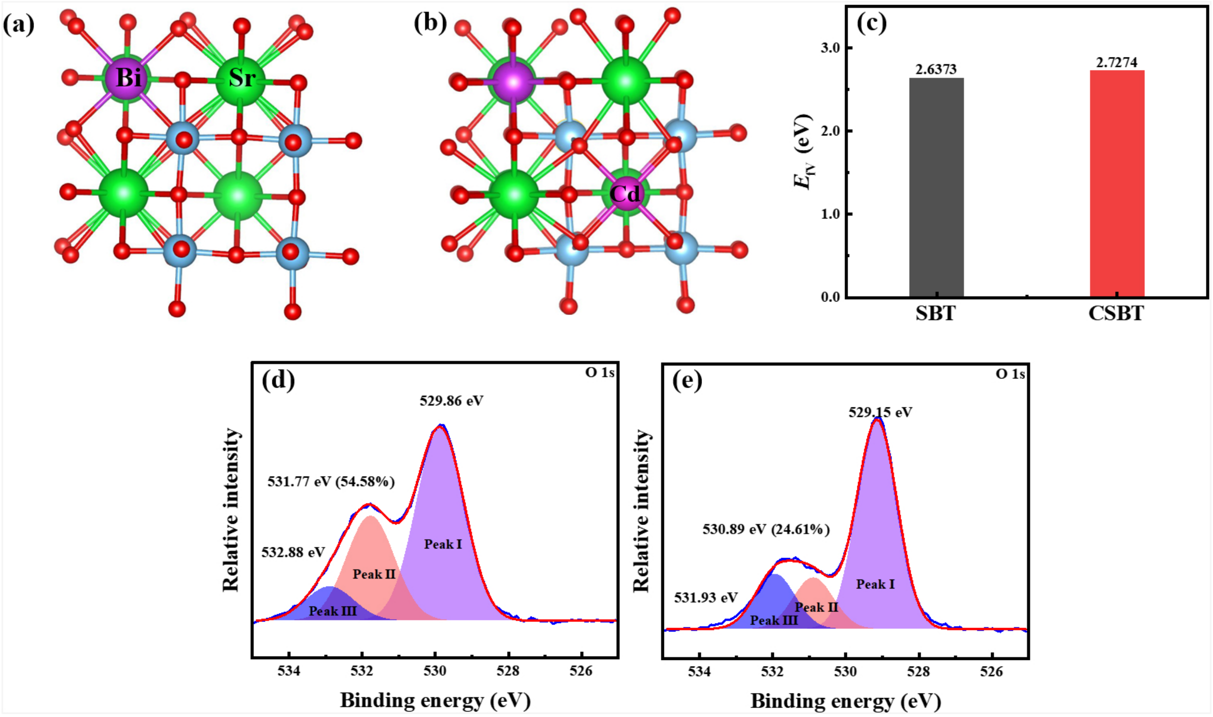

Fig. 6 (a, b) Crystal structure models of SBT and CSBT. (c) E_{fv} of SBT and CSBT. XPS spectra of the O 1s valance state for $\mathrm{Cd}_x\mathrm{Sr}_{0.775-x}\mathrm{Bi}_{0.15}\mathrm{TiO}_3$ with (d) $x = 0$ and (e) $x = 0.05$.

configurations, referred to as "images", was then generated with uniform spacing between these fixed endpoints. The MEP was subsequently searched by iteratively relaxing the elastic band toward zero forces while keeping the endpoints constrained. More specifically, the climbing-image NEB (CI-NEB) method was employed, which allows one of the images to converge precisely to the saddle point on the potential energy surface [44]. This approach significantly reduces the risk that the NEB procedure converges on an incorrect pathway that deviates from the true MEP. In all calculations (Fig. 7), five images were used, with each image assigned to an independent processor core via parallel computation within VASP. The computational results, as presented in Fig. 7, demonstrate that the energy barrier for oxygen vacancy migration is significantly increased upon Cd^{2+} doping (Fig. 7(b)) compared with the undoped system (Fig. 7(a)). This indicates that oxygen vacancy migration becomes more difficult in the doped material, which is attributed to the increased disorder and enhanced A–O bond strength of the material [23]. In summary, the incorporation of Cd^{2+} makes the formation and migration of oxygen vacancies in the ceramics more difficult, which enhances the E_{cond} and reduces the leakage current density, thereby reducing conductivity and improving the BDS. Furthermore, the reduced leakage current density results in lower strain and lower thermal dissipation, which contribute to higher η and enhanced device reliability [45].

In the enhancement of BDS influenced by various factors, the evolution of microscopic morphology is particularly crucial. The distribution of secondary phases and the difference in ε_r between phases affect the LEF in multiphase ceramics, which directly influences the BDS. To investigate this effect, LEF simulations were performed for representative samples with $x = 0.05$ and 0.2. As shown in Figs. 8(a)–8(f), the ε_r of the secondary phase was set to $\varepsilon_r = 103$ for $x = 0.2$, based on the reported ε_r of $Bi_2Ti_2O_7$, Sr_2TiO_4, and $Cd_{0.8}Sr_{0.2}TiO_3$ weighted by their corresponding volume fractions [46–48]. The primary phase of ε_r for $x = 0.2$ sample was set to 1455 (the detailed calculation procedure is shown in Fig. S7 and Table S1 in the ESM).

Due to the large ε_r contrast between the two phases, the applied electric field tends to concentrate more heavily in the low-ε_r secondary phase, leading to an inhomogeneous potential distribution and higher LEF. Comparing with the sample of $x = 0.05$, the $x = 0.2$ sample exhibits greater secondary-phase aggregation, resulting in more pronounced equipotential line distortions and a larger number of high-LEF regions (highlighted in red in Fig. 8(f)). The higher LEF in the $x = 0.2$ sample increases the breakdown probability. Meanwhile, when $x \geq 0.1$, the decreased E_{cond} and the leakage current density, and increased conductivity also lead to a declining trend in BDS [48,49].

3.4 Energy storage properties of CSBT

The unipolar P–E hysteresis loops of the CSBT ceramics at 120 kV/cm are shown in Fig. 9(a). All samples exhibit slim P–E loops with relatively low P_r, which reflects the fast response of PNRs and their excellent relaxor characteristics. As x increases, P_{max} decreases (Fig. 9(b)), and W_{rec} also decreases (Fig. S8 in the ESM). The reduction in P_{max} is attributed to increased secondary-phase content and the disruption of long-range ferroelectric order. Based on numerous studies on Sr_2TiO_4, $Cd_{0.8}Sr_{0.2}TiO_3$, and $Bi_2Ti_2O_7$, these secondary phases are likely to behave as dielectrics with low polarization [49–51]. Therefore, the increase in secondary phases is considered responsible for the reduction in P_{max}. CSBT ceramics exhibit bulge-shaped J–E loops with gentle slopes (Fig. 9(c)), indicating typical relaxor characteristics [52]. This phenomenon can be attributed to the switching of small sized PNRs or nanodomains under electric field.

The unipolar P–E loops of CSBT ceramics under critical electric fields are shown in Fig. 10(a). The critical electric field increases significantly with increasing x, rising from 310 kV/cm for $x = 0$ to 490 kV/cm for $x = 0.05$. Among the studied compositions, the sample with $x = 0.05$ exhibits the highest W_{rec} under high η (Fig. 10(b)). This outstanding performance originates from the combined effects of its high critical electric field, large P_{max}, and relatively small P_r. Such characteristics benefit from a moderate Cd^{2+} introduction, which enhances cation disorder and optimizes relaxor properties. This modification concurrently improves the BDS, thereby effectively enhancing the energy storage performance. Under an applied electric field of 490 kV/cm, the sample with $x = 0.05$ (CSBT05) exhibits a W of 5.56 J/cm^3, a W_{rec} of 5.16 J/cm^3, and an η of 92.66% (Figs. 10(c) and 10(d)). Its overall performance surpasses that of many recently reported Bi- or Sr-based ceramic systems (Fig. 10(e)), the specific data and related references are shown in ESM.

The practical application of energy-storage materials requires excellent stability against variations in temperature, frequency, and cycling. The P–E loops and energy-storage characteristics of the sample with $x = 0.05$ under different conditions are shown in Figs. 11(a)–11(c). All samples exhibit slim P–E loops with low P_r (Fig. S9 in the ESM), indicating superior relaxor stability. As the temperature increases (Fig. 11(d) and Fig. S9(a) in the ESM), P_{max} decrease slightly due to enhanced thermal fluctuations, reduced PNR size, and increased PNR dynamics [53]. As a result, W_{rec} shows a slight decrease, but the variations in both W_{rec} and η remain within a narrow range. Regarding frequency stability (Fig. 11(e) and Fig. S9(b) in the ESM), an increase in frequency leads to the slight improvement in W_{rec} and η with stable P_{max} and P_r, indicating relatively good frequency stability of the material. In terms of cycling stability (Fig. 11(f) and Fig. S9(c) in the ESM),

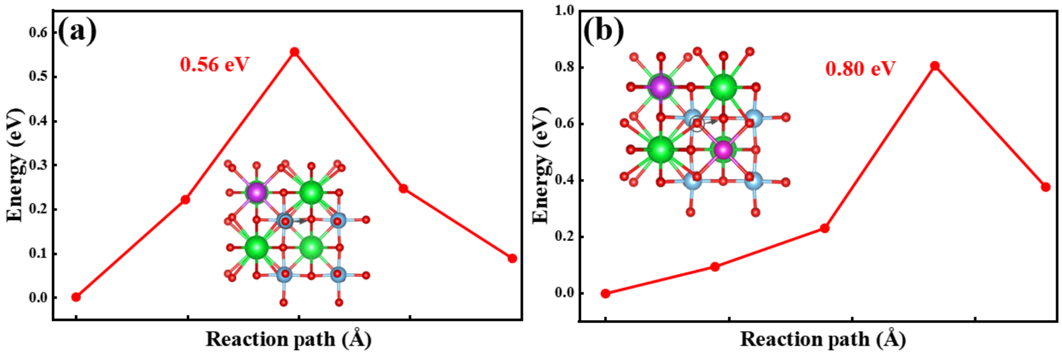

Fig. 7 Migration pathway and energy profile of oxygen vacancy migration in (a) SBT and (b) CSBT.

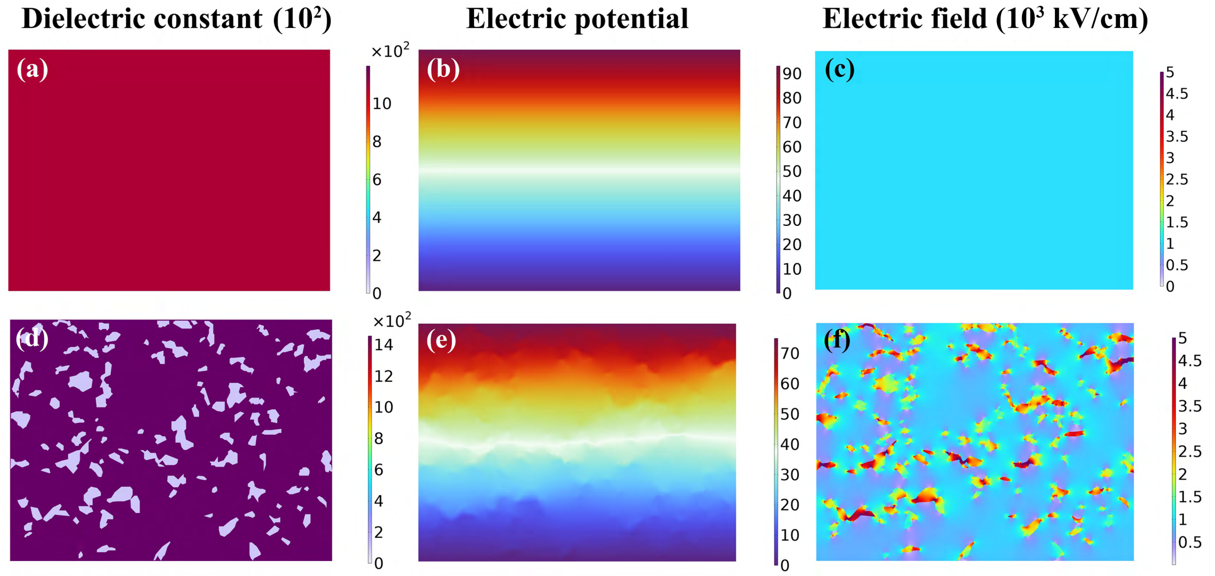

Fig. 8 Numerical simulation of distribution of ε_r of $\mathrm{Cd}_x\mathrm{Sr}_{0.775-x}\mathrm{Bi}_{0.15}\mathrm{TiO}_3$ with (a) $x = 0.05$ and (d) $x = 0.2$, distribution of electric potential of $\mathrm{Cd}_x\mathrm{Sr}_{0.775-x}\mathrm{Bi}_{0.15}\mathrm{TiO}_3$ with (b) $x = 0.05$ and (e) $x = 0.2$, and distribution of LEF of $\mathrm{Cd}_x\mathrm{Sr}_{0.775-x}\mathrm{Bi}_{0.15}\mathrm{TiO}_3$ with (c) $x = 0.05$ and (f) $x = 0.2$.

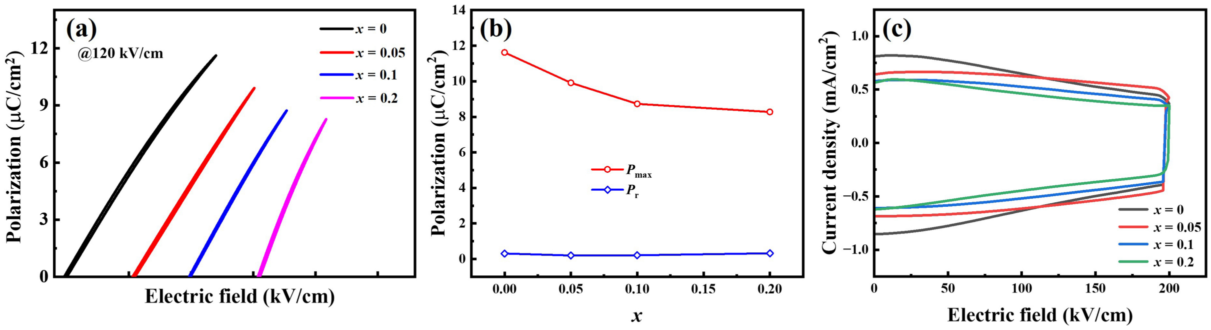

Fig. 9 (a) Unipolar P–E loops of $\mathrm{Cd}_x\mathrm{Sr}_{0.775-x}\mathrm{Bi}_{0.15}\mathrm{TiO}_3$ (x = 0, 0.05, 0.1, and 0.2) ceramics at 120 kV/cm and 10 Hz (each scale of the horizontal axis is 50 kV/cm). (b) P_{max} and P_{r} of $\mathrm{Cd}_x\mathrm{Sr}_{0.775-x}\mathrm{Bi}_{0.15}\mathrm{TiO}_3$ (x = 0, 0.05, 0.1, and 0.2) ceramics at 120 kV/cm and 10 Hz. (c) J–E loops of $\mathrm{Cd}_x\mathrm{Sr}_{0.775-x}\mathrm{Bi}_{0.15}\mathrm{TiO}_3$ (x = 0, 0.05, 0.1, and 0.2) ceramics at 200 kV/cm and 10 Hz.

after 10^6 cycles, P_{max} and P_{r} exhibit slight fluctuations, while W_{rec} and η show small change. Such excellent cycling endurance can be attributed to the highly dynamic nanoscale domain structure, dense microstructure, and reduced oxygen vacancy concentration. Notably, CSBT05 ceramics demonstrate outstanding temperature, frequency, and cycling stability, highlighting their significant potential for applications in harsh environments.

3.5 Pulsed charge–discharge performance of CSBT05

High power density, high discharge energy density, and fast charge–discharge rates are essential for the practical application of energy-storage ceramics in high-power devices. The overdamped current–time (I–t) curves of CSBT05 ceramics under different electric fields are presented in Fig. 12(a). As the electric field strength increases from 60 to 360 kV/cm, the current peak rises linearly from 1.96 to 11.45 A. The discharge energy density (W_{d}) can be calculated using Eq. (7):

$$W_{\mathrm{d}} = \frac{R\int i^2(t)\,\mathrm{d}t}{V} \tag{7}$$

where R denotes the load resistance (150 Ω), and V is the sample volume. The parameter $t_{0.9}$, defined as the time required to release 90% of W_{d}, is commonly employed to evaluate the discharge rate. As the applied electric field increases, W_{d} gradually increases, while $t_{0.9}$ relatively decreases (Fig. S10 in the ESM). Under an electric field of 360 kV/cm, the CSBT05 ceramic demonstrates outstanding discharge performance, with a W_{d} of 2.52 J/cm³ and an ultrafast $t_{0.9}$ of 0.046 μs (Fig. 12(b)). It is worth noting that the experimentally obtained W_{d} values are lower than the W_{rec} estimated from the P–E loops under the same electric field. This discrepancy primarily stems from energy dissipation in the equivalent series resistance and the increased viscous force associated with pinned domain walls during the charge–discharge process [54]. Furthermore, Fig. 12(c) illustrates the underdamped current–time (I–t) characteristics of the CSBT05 ceramics under different electric fields. The current density (C_{D}) and power density (P_{D}) can be calculated according to Eqs (8) and (9) [24]:

$$C_{\mathrm{D}} = \frac{I_{\mathrm{max}}}{S} \tag{8}$$

$$P_{\mathrm{D}} = \frac{EI_{\mathrm{max}}}{2S} \tag{9}$$

where I_{max} denotes the maximum discharge current, S is the electrode area, and E represents the applied electric field strength. At 360 kV/cm, the CSBT05 ceramic exhibits an outstanding performance, achieving a maximum I_{max} of 20.08 A, a C_{D} of 639.01 A/cm², and a P_{D} of 115.02 MW/cm³ (Fig. 12(d)).

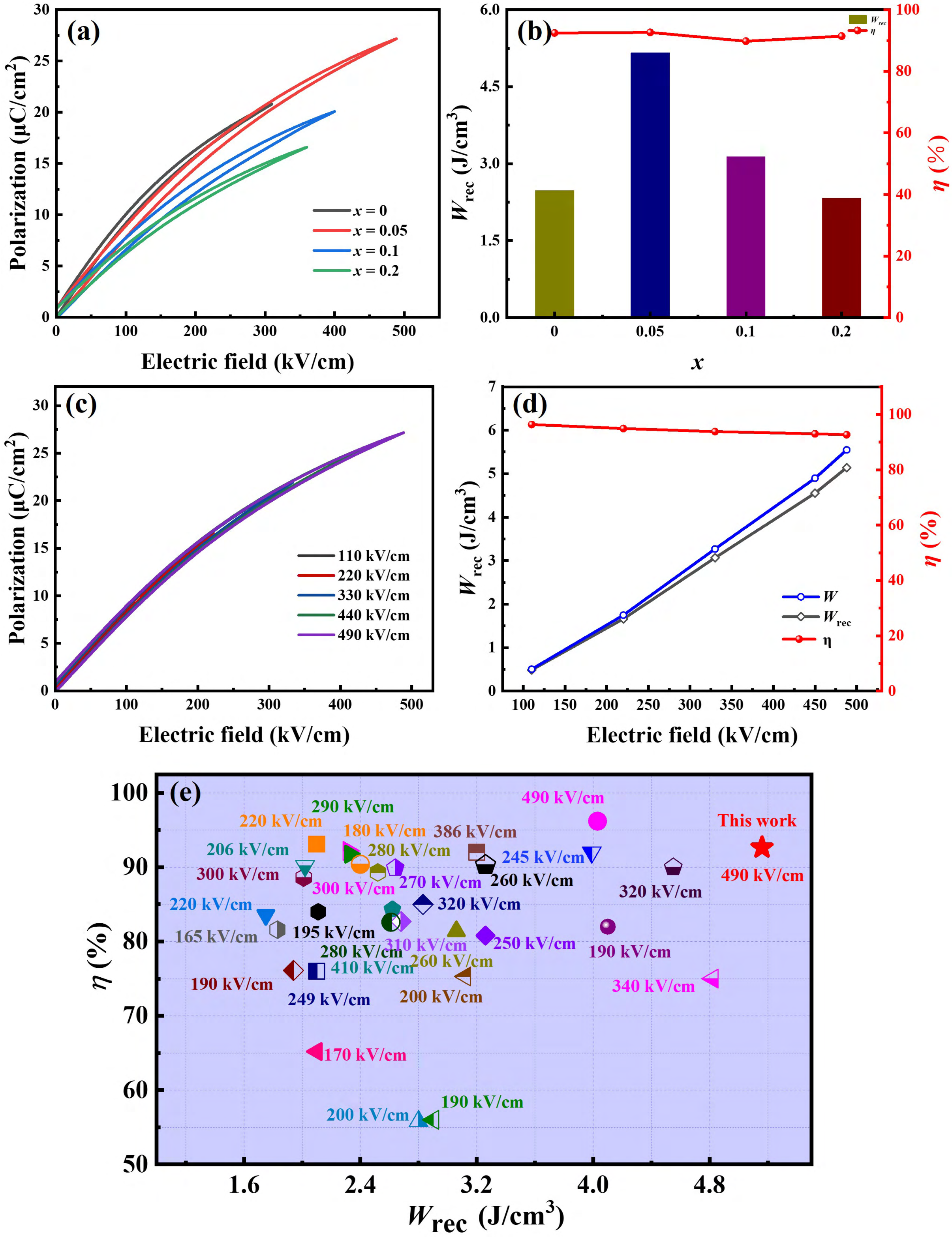

Fig. 10 (a) Unipolar P–E loops of CSBT100x (x = 0, 0.05, 0.1, and 0.2) ceramics with critical electric field at 10 Hz. (b) Energy storage properties of CSBT100x (x = 0, 0.05, 0.1, and 0.2) ceramics with critical electric field at 10 Hz. (c) Unipolar P–E loops of CSBT05 ceramics with different electric fields at 10 Hz. (d) Energy storage properties of CSBT05 ceramics with different electric fields at 10 Hz. (e) Comparison of energy storage properties of various energy storage ceramics.

Compared with other Bi- and Sr-based energy-storage ceramics, the CSBT05 composition simultaneously demonstrates superior W_d, P_D, and BDS (the specific data andrelated references are shown in the ESM), highlighting its significant potential for high-power energy-storage applications (Fig. 12(e)).

The overdamped current–time curves and the corresponding W_d values of CSBT05 ceramics at different temperatures are shown in Fig. 13(a). As the temperature varies, the samples display similar discharge behavior, and W_d fluctuates within the range of 0.63–0.76 J/cm³. Figure 13(b) also shows the underdamped current–time curves, I_{max}, C_D, and P_D, for CSBT05 ceramics at different temperatures. Owing to the dielectric nonlinearity at

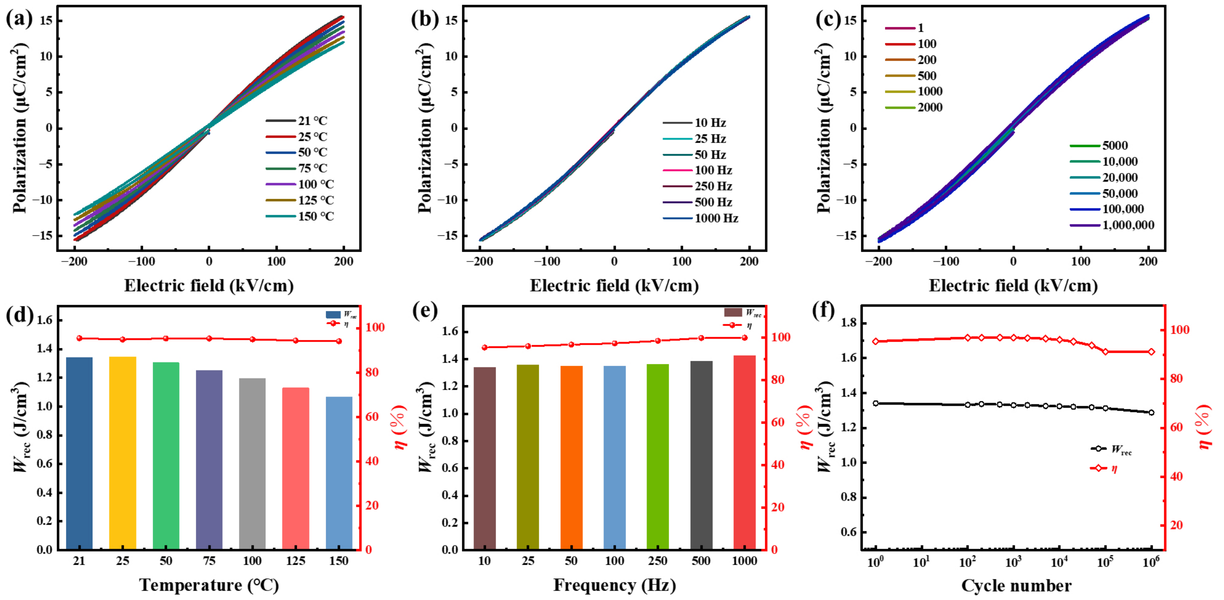

Fig. 11 (a–c) *P–E* loops of CSBT05 ceramics at different temperatures (21–150 °C, 10 Hz), frequencies (10–1000 Hz, 25 °C), and selected cycle numbers (1–10^6, 10 Hz, 25 °C) at 200 kV/cm. (d–f) Energy storage properties of CSBT05 ceramics with different temperatures (21–150 °C, 10 Hz), frequencies (10–1000 Hz, 25 °C), and selected cycle numbers (1–10^6, 10 Hz, 25 °C) at 200 kV/cm.

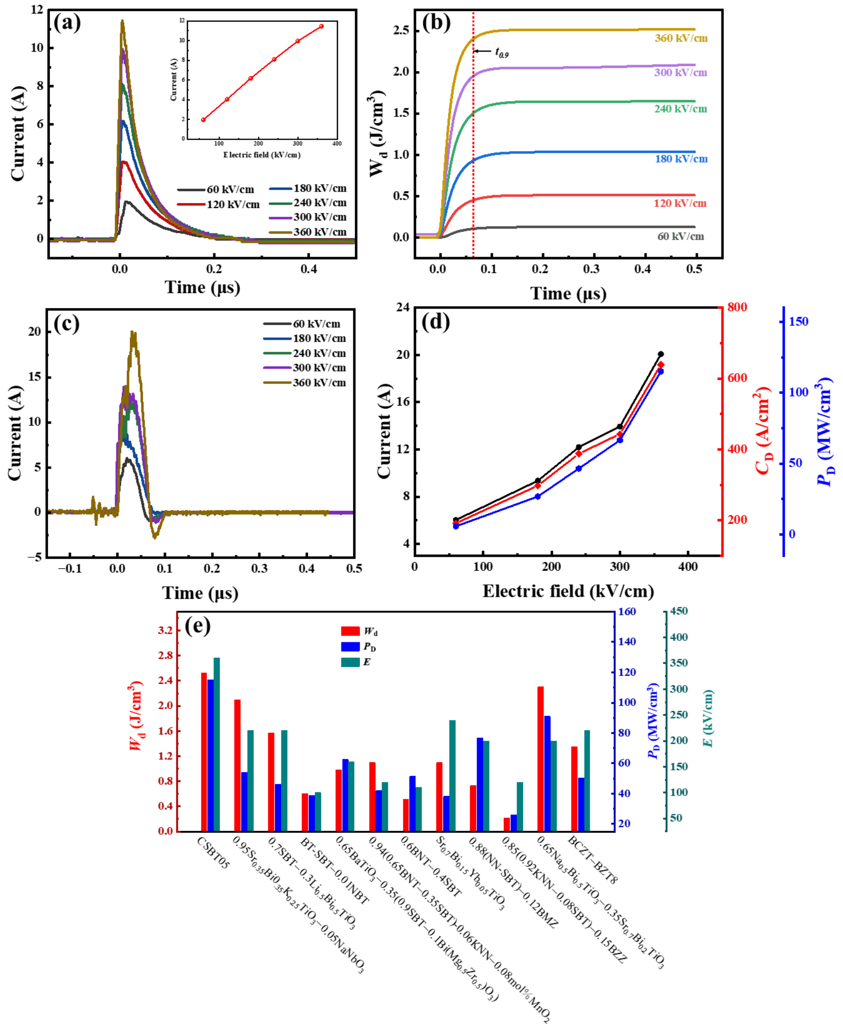

Fig. 12 (a) Overdamped current–time curves of CSBT05 under various electric fields (60–360 kV/cm); the inset shows change in current with different electric fields. (b) Time dependence of W_d of CSBT05 under various electric fields (60–360 kV/cm). (c) Underdamped current–time curves of CSBT05 under various electric fields (60–360 kV/cm). (d) Changes in I_{max}, C_D, and P_D of CSBT05 as functions of electric fields (60–360 kV/cm). (e) Comparison of charge–discharge performance of various energy storage ceramics.

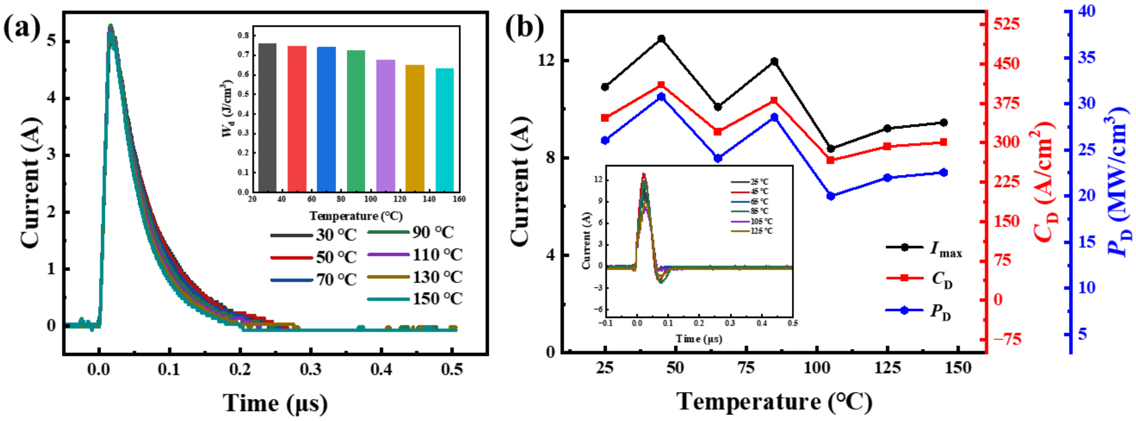

Fig. 13 (a) Overdamped current–time curves of CSBT05 at various temperatures (30–150 °C) at 150 kV/cm; inset shows change in energy storage properties with temperature at 150 kV/cm. (b) Changes in I_{max}, C_D, and P_D of CSBT05 as functions of temperature (25–150 °C) at 150 kV/cm; inset shows underdamped current–time curves of CSBT05 at various temperatures at 150 kV/cm.

different temperatures, the current peaks exhibit a relative shift. P_D remains relatively stable, with only minor variations in the range of 19.99–30.77 MW/cm³. These results indicate that CSBT05 ceramics possess excellent power characteristics and reliable temperature stability, highlighting their strong potential for practical high-power applications.

4 Conclusions

In summary, the comprehensive energy storage performance of SBT ceramics was effectively improved by Cd^{2+} doping at the A-site based on a multi-scale synergistic optimization strategy. At the nanoscale, first-principles calculations reveal that Cd^{2+} doping suppresses the formation of oxygen vacancies and concurrently increases the energy barrier for their migration. This is attributed to the decreased lattice volume and enhanced A–O bond strength and is verified by electrical testing and structural characterization. Meanwhile, Cd^{2+} doping enhanced ionic disorder. These factors suppressed oxygen vacancy transport dynamics and reduced conductivity. At the microscale, a pure phase was successfully prepared in CSBT05, and numerical simulation reveals that this sample possesses low and uniform LEF, resulting in a small breakdown probability. Furthermore, the relaxor ferroelectric behavior is enhanced after the introduction of Cd^{2+}, which maintains the P_r of the sample at a low level. As a result, CSBT05 achieves a high W_{rec} of 5.16 J/cm³ and an η of 92.66% at 490 kV/cm. Meanwhile, the ceramic exhibits an outstanding P_D of 115.02 MW/cm³ with a high current density and ultrafast charge–discharge rates. These remarkable characteristics demonstrate its promising potential for high-power applications. Moreover, CSBT05 demonstrates outstanding thermal, frequency, and cycling stability, underscoring its strong potential for use in advanced pulsed power and energy-storage devices under harsh conditions.

Acknowledgements

The authors greatly acknowledge the financial support from the the China Postdoctoral Science Foundation (No. 2024M762333), Guangxi Science and Technology Plan Project (GuikeAD25069100), National Natural Science Foundation of China (No. 52302147), the Fundamental Research Program of Shanxi Province (No. 202303021222013), and the National Key R&D Program of China (No. 2025YFF0521300).

Author contributions

Peng Zhao: supervised and directed the project, participated in the planning of research, designed and carried out the research, analyzed the experimental data, and wrote a draft of the manuscript. Yubin Liu: carried out the research, analyzed the experimental data, and wrote a draft of the manuscript. Jingjing Chen: designed and carried out the research, analyzed the experimental data, participated in some experiments, and took part in discussions. Yongjia Zhang and Bo Chen: carried out the first-principles calculations and contributed to the analysis and writing of the first-principles calculation section of the manuscript. Bin Tang: directed some experiments, participated in some data analysis, and contributed to the article language and writing. Yinhui Li, Chenguang Niu, Yongzhen Wang, and Xiaoyan Xiong: contributed to the article language and writing.

Availability of data and materials

The data that support the findings of this study are available from the corresponding author upon reasonable request.

Competing interests

The authors have no competing interests to declare that are relevant to the content of this article.

Electronic Supplementary Material

Supplementary material is available in the online version of this article at https://doi.org/10.26599/JAC.2026.9221314.

References

[1] Qiao XS, Wu D, Zhang FD, *et al.* Enhanced energy density and thermal stability in relaxor ferroelectric $Bi_{0.5}Na_{0.5}TiO_3$–$Sr_{0.7}Bi_{0.2}TiO_3$ ceramics. *J Eur Ceram Soc* 2019, **39**: 4778–4784.

[2] Xie B, Li ZQ, Luo HJ, *et al.* Constructing superrelaxor critical state towards giant energy storage in lead-free dielectric ceramics. *Nat Commun* 2026, **17**: 1583.

[3] Zhang XQ, Pu YP, Ning YT, *et al.* Ultrahigh energy storage with superfast charge–discharge capability achieved in linear dielectric ceramic. *J Mater Sci Technol* 2024, **177**: 59–67.

[4] Tong S, Ma BH, Narayanan M, *et al.* Lead lanthanum zirconate titanate ceramic thin films for energy storage. *ACS Appl Mater Inter* 2013, **5**: 1474–1480.

[5] Xie B, Wu QQ, Yu C, *et al.* Local structure strategies promoting lead-free dielectric energy-storage applications. *Small* 2026, **22**: e12097.

[6] Long CB, Su ZQ, Xu AW, *et al.* High energy storage performance in

the $Bi_{0.5}Na_{0.5}TiO_3$–$BaTiO_3$–$Nd(Mg_{1/2}Hf_{1/2})O_3$ ternary system with multiscale polymorphic domains and local heterogeneous structure. *J Adv Ceram* 2025, **14**: 9221063.

[7] He S, Lou KJ, Han B, *et al.* Superior energy storage density and efficiency in antiferroelectric-like BNT-based ceramics via single-element phase engineering. *J Adv Ceram* 2025, **14**: 9221056.

[8] Dai SW, Li MY, Wu XW, *et al.* Combinatorial optimization of perovskite-based ferroelectric ceramics for energy storage applications. *J Adv Ceram* 2024, **13**: 877–910.

[9] Yang KH, Luo GG, Ma L, *et al.* Excellent energy storage performance in $Bi_{0.5}Na_{0.5}TiO_3$-based lead-free high-entropy relaxor ferroelectrics via B-site modification. *J Adv Ceram* 2024, **13**: 345–353.

[10] He B, Zhou B, Yan SG, *et al.* Ultrahigh energy density and efficiency $BaTiO_3$-based multilayer ceramic capacitors. *J Adv Ceram* 2025, **14**: 9221018.

[11] Yao K, Zhou CR, Wang J, *et al.* A new strategy to realize high energy storage properties and ultrafast discharge speed in $Sr_{0.7}Bi_{0.2}TiO_3$-based relaxor ferroelectric ceramic. *J Alloy Compd* 2021, **883**: 160855.

[12] Chen JJ, Zhao P, Si F, *et al.* Dielectric, energy storage, and charge–discharge properties of Yb-modified $Sr_{0.7}Bi_{0.2}TiO_3$ relaxor ferroelectric ceramic. *J Am Ceram Soc* 2024, **107**: 2504–2516.

[13] Chen JJ, Zhao P, Si F, *et al.* Optimizing electrical performance of low hysteresis $Sr_{0.7}Bi_{0.2}TiO_3$ energy storage ceramic. *Ceram Int* 2024, **50**: 13208–13218.

[14] Li YF, Zeng MS, Tan FH, *et al.* Enhanced breakdown strength and excellent energy storage stability by B site hetero-valent doping in $Sr_{0.7}Bi_{0.2}TiO_3$-based lead-free ceramic. *J Alloy Compd* 2023, **947**: 169504.

[15] Li YF, Liu JS, Zeng MS, *et al.* Relaxor properties and breakdown strength of Ta doped $Sr_{0.7}Bi_{0.2}TiO_3$-based lead-free ceramics for energy storage applications. *J Mater Sci* 2023, **58**: 16195–16207.

[16] Chen JJ, Zhao P, Si F, *et al.* Simultaneously achieving high energy storage and charge–discharge performance by Nd-doped $Sr_{0.7}Bi_{0.2}TiO_3$ lead-free relaxor ferroelectric ceramics. *J Alloy Compd* 2023, **966**: 171354.

[17] Li YF, Liu JS, Zeng MS, *et al.* Enhanced relaxor behavior and excellent anti-fatigue performance in lanthanum-modified $Sr_{0.7}Bi_{0.2}TiO_3$ ceramics. *Mater Today Commun* 2024, **41**: 110872.

[18] Chen JJ, Zhao P, Chen K, *et al.* Aliovalent doping engineering to synergistically optimize the energy storage properties of $Sr_{0.7}Bi_{0.2}TiO_3$-based linear-like relaxor ferroelectric ceramics. *Chem Eng J* 2024, **502**: 157866.

[19] Song BJ, Wu SH, Li F, *et al.* Excellent energy storage density and charge–discharge performance of a novel $Bi_{0.2}Sr_{0.7}TiO_3$–$BiFeO_3$ thin film. *J Mater Chem C* 2019, **7**: 10891–10900.

[20] Ang C, Yu Z. High, purely electrostrictive strain in lead-free dielectrics. *Adv Mater* 2006, **18**: 103–106.

[21] Padmini E, Ramachandran K. Investigation on versatile behaviour of Cd doped $SrTiO_3$ perovskite structured compounds. *Solid State Commun* 2019, **302**: 113716.

[22] Rafiq MN, Dai ZH, Zheng YY, *et al.* Enhanced energy storage properties of Cd-doped $(Pb,La)(Sn,Zr,Ti)O_3$ ceramics for pulsed power capacitors. *J Power Sources* 2025, **660**: 238563.

[23] Guo J, Yu HF, Ren YF, *et al.* Multi-symmetry high-entropy relaxor ferroelectric with giant capacitive energy storage. *Nano Energy* 2023, **112**: 108458.

[24] Zhao P, Chen JJ, Chen K, *et al.* Structure regulation and performance optimization mechanism of $Sr_{0.7}Bi_{0.2}TiO_3$-based energy storage ceramics based on charged defect design engineering. *Chem Eng J* 2024, **500**: 156673.

[25] Wu QQ, Luo HJ, Hu YH, *et al.* Hierarchical polar–nonpolar phase architecture enabling excellent lead-free capacitive energy storage. *Chem Sci* 2026, **17**: 8701–8711.

[26] Xiong X, Shi YB, Zhang J, *et al.* Giant energy-storage in Pb-free relaxor ferroelectrics via atomic-level design. *Adv Mater* 2026, **38**: e17815.

[27] Zhao P, Tang B, Si F, *et al.* Novel Ca doped $Sr_{0.7}Bi_{0.2}TiO_3$ lead-free relaxor ferroelectrics with high energy density and efficiency. *J Eur Ceram Soc* 2020, **40**: 1938–1946.

[28] Shannon RD. Revised effective ionic radii and systematic studies of interatomic distances in halides and chalcogenides. *Acta Crystallogr A* 1976, **32**: 751–767. (in Chinese)

[29] Shi J, Fan HQ, Liu X, *et al.* Large electrostrictive strain in $(Bi_{0.5}Na_{0.5})TiO_3$–$BaTiO_3$–$(Sr_{0.7}Bi_{0.2})TiO_3$ solid solutions. *J Am Ceram Soc* 2013, **97**: 848–853.

[30] Schütz D, Deluca M, Krauss W, *et al.* Lone-pair-induced covalency as the cause of temperature- and field-induced instabilities in bismuth sodium titanate. *Adv Funct Mater* 2012, **22**: 2285–2294.

[31] Maqbool A, Hussain A, Ur Rahman J, *et al.* Enhanced electric field-induced strain and ferroelectric behavior of $(Bi_{0.5}Na_{0.5})TiO_3$–$BaTiO_3$–$SrZrO_3$ lead-free ceramics. *Ceram Int* 2014, **40**: 11905–11914.

[32] Liao QW, Li LX. Structural dependence of microwave dielectric properties of ixiolite structured $ZnTiNb_2O_8$ materials: Crystal structure refinement and Raman spectra study. *Dalton T* 2012, **41**: 6963–6969.

[33] Su YC, Zhou XF, Xue GL, *et al.* Temperature-stable $Na_{0.5}Bi_{0.5}TiO_3$-based ceramics with favorable low-temperature dielectric and energy storage property. *J Am Ceram Soc* 2023, **106**: 3525–3536.

[34] Li F, Zhai JW, Shen B, *et al.* Influence of structural evolution on energy storage properties in $Bi_{0.5}Na_{0.5}TiO_3$–$SrTiO_3$–$NaNbO_3$ lead-free ferroelectric ceramics. *J Appl Phys* 2017, **121**: 054103.

[35] Xu LY, Ouyang J, Cheng ZX, *et al.* A review on the dielectric ceramics for high energy-storage application. *Adv Ceram* 2025, **46**: 195–246. (in Chinese)

[36] Yang ZT, Du HL, Jin L, *et al.* Realizing high comprehensive energy storage performance in lead-free bulk ceramics via designing an unmatched temperature range. *J Mater Chem A* 2019, **7**: 27256–27266.

[37] Dai ZH, Xie JL, Fan X, *et al.* Enhanced energy storage properties and stability of $Sr(Sc_{0.5}Nb_{0.5})O_3$ modified $0.65BaTiO_3$–$0.35Bi_{0.5}Na_{0.5}TiO_3$ ceramics. *Chem Eng J* 2020, **397**: 125520.

[38] Li F, Zhai JW, Shen B, *et al.* Simultaneously high-energy storage density and responsivity in quasi-hysteresis-free Mn-doped $Bi_{0.5}Na_{0.5}TiO_3$–$BaTiO_3$–$(Sr_{0.7}Bi_{0.2}\ _{0.1})TiO_3$ ergodic relaxor ceramics. *Mater Res Lett* 2018, **6**: 345–352.

[39] Zhao NS, Fan HQ, Ning L, *et al.* Temperature-stable dielectric and energy storage properties of $La(Ti_{0.5}Mg_{0.5})O_3$-doped $(Bi_{0.5}Na_{0.5})TiO_3$–$(Sr_{0.7}Bi_{0.2})TiO_3$ lead -free ceramics. *J Am Ceram Soc* 2018, **101**: 5578–5585.

[40] Shi CM, Qin HW, Li L, *et al.* CO_2 sensing characteristics and mechanism for $LaCoO_3$ predicted by density function theory. *Appl Surf Sci* 2015, **327**: 168–173.

[41] Sun LH, Li GP, Chen W, *et al.* Adsorption of CO on the $LaCoO_3$(001) surface by density functional theory calculation. *Appl Surf Sci* 2014, **309**: 128–132.

[42] Zhang LP, Bredeson I, Birenbaum AY, *et al.* Oxygen vacancy formation energies in $PbTiO_3/SrTiO_3$ superlattice. *Phys Rev Mater* 2018, **2**: 064409.

[43] Tse MY, Wei XH, Hao JH. High-performance colossal permittivity materials of (Nb + Er) co-doped TiO_2 for large capacitors and high-energy-density storage devices. *Phys Chem Chem Phys* 2016, **18**: 24270–24277.

[44] Henkelman G, Uberuaga BP, Jónsson H. A climbing image nudged elastic band method for finding saddle points and minimum energy paths. *J Chem Phys* 2000, **113**: 9901–9904.

[45] Yang CH, Qian J, Han YJ, *et al.* Ni doping to enhance ferroelectric, energy-storage and dielectric properties of lead-free NBT ceramic thin film with low leakage current. *Ceram Int* 2018, **44**: 7245–7250.

[46] Sui HT, Yang DM, Jiang H, *et al.* Preparation and electrical properties of Sm-doped $Bi_2Ti_2O_7$ thin films prepared on Pt(111) substrates. *Ceram Int* 2013, **39**: 1125–1128.

[47] Viennois R, Hermet P, Machon D, *et al.* Stability and lattice

dynamics of ruddlesden–popper tetragonal Sr_2TiO_4. *J Phys Chem C* 2020, **124**: 27882–27893.

[48] Shan YJ, Mori H, Wang RP, *et al.* Powder X-ray diffraction study of ferroelectric phase transition in perovskite oxide $CdTiO_3$. *Ferroelectrics* 2001, **259**: 85–90.

[49] Kumar A, Prakash J, Varshney D, *et al.* Tailoring the dielectric features of a cyanobiphenyl based liquid crystal using bismuth titanate ($Bi_2Ti_2O_7/Bi_4Ti_3O_{12}$) nanocomposite. *Indian J Phys* 2025, **99**: 2485–2500.

[50] Ahmad T, Ganguli AK. Reverse micellar route to nanocrystalline titanates ($SrTiO_3$, Sr_2TiO_4, and $PbTiO_3$): Structural aspects and dielectric properties. *J Am Ceram Soc* 2006, **89**: 1326–1332.

[51] Ullah HMN, Rizwan M, Zahid U, *et al.* A comprehensive DFT study of physical and photocatalytic properties of $Sr_{1-x}Cd_xTiO_3$. *Mater Today Commun* 2022, **33**: 104495.

[52] Zhou MX, Liang RH, Zhou ZY, *et al.* Achieving ultrahigh energy storage density and energy efficiency simultaneously in sodium niobate-based lead-free dielectric capacitors via microstructure modulation. *Inorg Chem Front* 2019, **6**: 2148–2157.

[53] Huang JH, Qi H, Gao Y, *et al.* Expanded linear polarization response and excellent energy-storage properties in $(Bi_{0.5}Na_{0.5})TiO_3$–$KNbO_3$ relaxor antiferroelectrics with medium permittivity. *Chem Eng J* 2020, **398**: 125639.

[54] Hu D, Pan ZB, Zhang X, *et al.* Greatly enhanced discharge energy density and efficiency of novel relaxation ferroelectric BNT–BKT-based ceramics. *J Mater Chem C* 2020, **8**: 591–601.